Chapter 5
Methods of Cavity-Enhanced Laser Absorption Spectroscopy Using Microresonator Whispering-Gallery Modes

A. T. Rosenberger

Abstract Theoretical analysis of, and experimental results using, chemical sensing techniques based on microcavity-enhanced optical absorption are presented. Two methods are described in detail, and several extensions and enhancements of these methods are discussed briefly. Both techniques involve novel applications of tunable diode laser absorption spectroscopy in which cavity enhancement is provided by a dielectric microresonator (<1 mm in diameter) with whispering-gallery modes (WGMs) excited by tapered-fiber coupling. The evanescent component of a WGM allows for interaction with the analyte. The first method is used for the detection of trace gases in the ambient air by measuring the coupling-fiber throughput as the laser scans in frequency. Centimeter effective absorption path lengths are measured, in agreement with theory. The second method employs the observation of thermal bistability to enable measurement of absorption due to a coating applied to, or molecules adsorbed on, the microresonator's surface. Absorption by the water layer on a fused-silica surface agrees with theory, and results for thermal accommodation coefficients and thin-film absorption are also presented.

5.1   Introduction

Dielectric microresonators supporting whispering-gallery modes (WGMs) are becoming increasingly useful for numerous applications in optics. These resonators, often made of fused silica because of its extremely low absorption and scattering losses, can be spherical, cylindrical, disk-shaped, or toroidal; they are typically a few hundred μm in diameter. Light in a WGM circulates around the circumference of the resonator, localized near the surface (for example, at the equator of a sphere) by total internal reflection. The impact of these devices is based on certain attractive

A.T. Rosenberger
Department of Physics, Oklahoma State University, Stillwater, OK 74078-3072, USA
e-mail: atr@okstate.edu

properties of WGMs, such as high quality factor (Q) and low mode volume, and on the possibility of efficient coupling of light into and out of these modes[1]. The high Q of a WGM means that light makes many round trips in the resonator before being lost from the mode by outcoupling, scattering, or absorption. This feature, combined with small mode volume and efficient coupling using prisms, angle-polished fibers, or tapered fibers, makes high intracavity power enhancement easy to achieve. Various applications such as filtering, lasing, modulation, nonlinear optics, sensing, and spectroscopy are enabled by these properties of WGMs[2].

Part of the WGM field extends outside the dielectric, and it is this evanescent portion that interacts with the surrounding medium or with a surface layer, making the WGM a sensitive probe of the microresonator's environment. Two sensing methods will be described here. The first method is microcavity-enhanced laser absorption spectroscopy of molecules in the ambient gas or liquid[3,4], to be discussed in the following three sections. Section 5.2 will give a theoretical analysis of the operation of a chemical sensor based on this technique; Section 5.3 will present results for its use in detection of atmospheric trace gases; and a discussion of possible extensions and enhancements will follow in Sect. 5.4. The second method is based on using the temperature sensitivity of WGM resonance frequencies to characterize surfaces and thin films[5]. Section 5.5 is devoted to this technique, and in Sect. 5.6 the chapter concludes with a summary and outlook.

5.2 Theoretical Analysis of Microcavity-Enhanced Absorption Sensors

In the application area of label-free chemical detection and spectroscopy, several different methods of using WGM microresonators have previously been reported. Analyte molecules in the ambient gas or liquid or on the resonator's surface can be detected by measuring the frequency shift of a WGM caused by the analyte's perturbation of the ambient's index of refraction[6,7]. In addition, analyte absorption will change the effective Q of the WGM, and the associated modification of mode linewidth can be measured[8]. One can also envision using cavity-ringdown spectroscopy[9]. The method described in this section is more closely related to other earlier work[10] in which what is measured is the analyte absorption effect, for continuous-wave input, on either the depth of the throughput dip or the strength of the drop signal. As explained below, dip-depth detection can be more sensitive than other tunable single-frequency methods, and drop-signal detection lends itself well to broadband spectroscopy.

5.2.1 Tunable Single-Frequency Operation

Consider a microcavity in which light is coupled into a WGM from an adiabatically tapered fiber tangentially in contact with the resonator. Tunable single-frequency
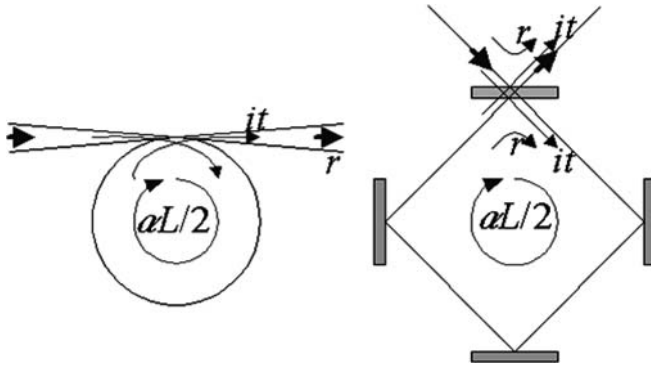
Fig. 5.1 Four-mirror ring cavity model. *Left*, microcavity and tapered fiber in contact. Light can couple from the fiber into the resonator and back into the fiber. *Right*, the four-mirror ring cavity equivalent. The top mirror is partially transmitting; all others have 100% reflectivity. Reprinted from Ref. 3 with permission. © 2008 Optical Society of America

light is injected at one end of the tapered fiber and the throughput spectrum is detected at the other end. The throughput will display a Lorentzian dip for each WGM resonance that is excited, because some power is lost to scattering and absorption in the resonator's WGM.

The microcavity can be modeled as a four-mirror ring cavity, as depicted in Fig. 5.1, in which one of the mirrors is partially transmitting while all the others are assumed to be perfect reflectors. The ring cavity model is a valid analog to a fiber-coupled microresonator when only a single fiber mode is excited. For light incident on a microresonator, this is accomplished by making the first fiber taper transition adiabatic. However, light coupling out of the microresonator can couple into many fiber modes, and any light coupled into higher-order modes will be lost if the second taper transition is also adiabatic. Fortunately, it is possible to make this lossy coupling into higher-order fiber modes negligibly small by properly choosing the diameter of the tapered fiber[11].

A round-trip power loss αL, where α is the loss coefficient and L is the micro-resonator circumference, is assumed; it models the intrinsic loss (primarily surface scattering) of a WGM microresonator. The reflection and transmission coefficients r and it, relating to the field mode amplitudes, are taken to be real and imaginary, respectively, without loss of generality; this corresponds to the usual choice for fiber or prism coupling[10,12,13]. The assumption of negligible power loss into radiation modes requires that these coefficients satisfy the relation $t^2 = 1 - r^2$. Because Q is so high, even under conditions of loading by the coupler, the intrinsic round-trip loss and the coupling loss (mirror transmissivity or probability of photon tunneling between fiber and microresonator) will always be small, so $\alpha L \ll 1$ and $T = t^2 \ll 1$ will be assumed throughout this chapter.

By summing the field over round trips, the net reflected power fraction (fiber throughput fraction) is found to be

$$R_\delta = \left| \frac{r - e^{-\alpha L/2}e^{i\delta}}{1 - r\,e^{-\alpha L/2}e^{i\delta}} \right|^2, \tag{5.1}$$

where $\delta = 2\pi nL(v - v_0)/c$ is the round-trip phase accumulation due to detuning of the input frequency v from resonance v_0 (c is the speed of light and n is the resonator's index of refraction). The deviation of the throughput fraction from unity gives the dip profile:

$$M_\delta = 1 - R_\delta = \frac{T\alpha L}{\frac{1}{4}(T + \alpha L)^2 + 4\sin^2\frac{1}{2}\delta} \cong \frac{T\alpha L}{\frac{1}{4}(T + \alpha L)^2 + \delta^2}. \tag{5.2}$$

This function is the usual Airy profile, with maxima at $\delta = p2\pi, p = 0, 1, 2, \ldots$. The spacing of 2π between adjacent modes is the free spectral range (FSR) in phase. (Recall that the FSR in frequency is given to good approximation by $c/(nL)$. Because many higher-order WGMs can be excited, the actual spacing between adjacent modes is much less than the FSR.) The full width at half-maximum of a WGM resonance is thus seen to be given by $\Delta\delta = T + \alpha L$, the total round-trip loss. The final expression in (5.2), valid when $\delta \ll 1$, shows the Lorentzian profile of a dip.

The dip depth on resonance ($\delta = 0$) is determined by the ratio of the coupling loss to intrinsic loss, $x = T/\alpha L$, and is given by

$$M_0 = \frac{4x}{(1 + x)^2}. \tag{5.3}$$

If $x = 1$, critical coupling is obtained and the dip depth attains its maximum value of 100%; the microresonator is said to be undercoupled if $x < 1$ and overcoupled for $x > 1$. While the coupling loss remains constant, the effective intrinsic loss can be changed by interaction of the evanescent fraction (f) of the WGM with the surrounding medium. The effective loss coefficient can then be written as $\alpha = \alpha_i + f\alpha_a + f\alpha_s$, where the three terms denote true intrinsic loss, absorption (and perhaps also scattering) by the analyte, and absorption in the solvent (or ambient).

Absorption by the analyte causes a change in dip depth that, when small (weak analyte absorption), is proportional to the change in analyte absorption coefficient, in analogy with Beer's law. A theoretical effective absorption path length L_{eff}^t can then be obtained from the dip-depth dependence on the absorption coefficient of the analyte

$$\frac{dM_0}{M_0} \cong -\left(\frac{1 - x}{1 + x}\right)\frac{f}{\alpha_i + f\alpha_s}d\alpha_a \cong -L_{eff}^t d\alpha_a. \tag{5.4}$$

In the absence of solvent absorption, this effective absorption path length can be expressed as

$$L_{eff}^t = \left(\frac{1-x}{1+x}\right)\frac{f}{\alpha_i}. \tag{5.5}$$

This effective length is defined in the low-analyte-absorption limit, $\alpha_a L_{eff}^t \ll 1$ (or $f\alpha_a \ll \alpha_i$), which is the condition for (5.4) to hold. Note that in the strongly undercoupled or overcoupled limits ($x \ll 1$ or $x \gg 1$) the relative detection sensitivity is determined by the intrinsic loss only. This can be advantageous, since having the tapered fiber in contact with the microresonator tends to produce overcoupling, especially when the system is immersed in a liquid. Thus in the strongly overcoupled case, this method has greater relative sensitivity (here, fractional change in dip depth) than the frequency-shift, mode-width, or ringdown methods, all of whose relative sensitivities are determined by the total loss. Recall that the total loss determines the linewidth and the cavity lifetime, and in the overcoupled limit coupling loss dominates. The relative frequency-shift sensitivity is measured as a fraction of the full linewidth, the change in mode width is relative to the full width, and ringdown measures the fractional change in the overall lifetime; however, the relative change in dip depth depends on the ratio of analyte absorption to intrinsic loss only.

An experimental effective absorption path length L_{eff}^e can be found by measuring the dip depth in the absence of analyte (M_0) and in the presence of analyte ($M_0 + \Delta M_0$)

$$L_{eff}^e \cong \frac{1}{\alpha_a}\ln\frac{M_0}{M_0 + \Delta M_0}. \tag{5.6}$$

As with (5.4), this holds for small changes in dip depth or $\alpha_a L_{eff}^e \ll 1$. Comparison of experimental and theoretical effective absorption path lengths for detection of atmospheric trace gases shows good agreement[4], as discussed in Sect. 5.3.

This method also allows for sensitive detection of an analyte in a strongly absorbing solvent. In (5.4), if $f\alpha_s \gg \alpha_i$, the effective absorption path length can still be as large as $1/\alpha_s$. In effect, solvent absorption can shift the sensor from one sensitive regime to another – from strongly overcoupled to strongly undercoupled, enabling absolute analyte sensitivity, i.e., actual signal amplitudes, that would be difficult to achieve in single-pass direct absorption through the same effective path length.

5.2.2   Broadband Operation

In modeling this mode of operation, a microsphere, with a prism coupler used to excite precessing modes[14], is taken to be analogous to a ring cavity with two identical partially transmitting mirrors. Here we will concentrate on the transmitted signal (drop power output, enabled by precession and detected by a spectrometer) rather than the reflected signal (throughput) (see Fig. 5.2).
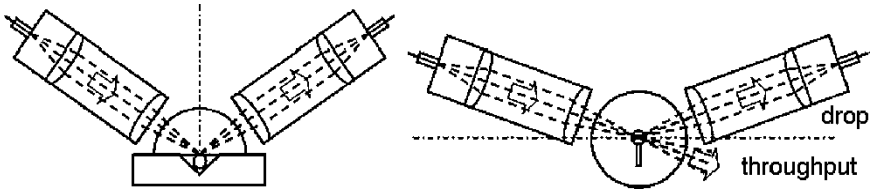
Fig. 5.2 Hemispherical prism coupling scheme. The microsphere is in a V-groove channel for the solvent and analyte. *Left*, polar view showing input and output coupling. *Right*, equatorial view illustrating how precessed light is collected at the drop port. Reprinted from Ref. 3 with permission © 2008 Optical Society of America

First consider single-frequency response. Summing over round trips and arbitrarily taking the second partially transmitting mirror to be at half the round-trip distance from the input mirror (the final result will not depend on this choice), gives the drop power fraction

$$D_\delta = \left| \frac{T \, e^{-\alpha L/4} e^{i\delta/2}}{1 - r^2 e^{-\alpha L/2} e^{i\delta}} \right|^2 = \frac{T^2}{\left(T + \frac{1}{2}\alpha L\right)^2 + 4\sin^2 \frac{1}{2}\delta} = D_0 \frac{\left(\frac{1}{2}\Delta\delta\right)^2}{\left(\frac{1}{2}\Delta\delta\right)^2 + \left(2\sin\frac{1}{2}\delta\right)^2}. \quad (5.7)$$

In this system, the mode width is $\Delta\delta = 2T + \alpha L$ and the resonant drop fraction is D_0.

Now, consider the case where the input is broadband and the drop signal is detected by a spectrometer, which integrates over a frequency interval that we will take to be equal to the FSR (for convenience; again, the final result will not depend on this choice, and the spectrometer resolution interval may be greater than or less than the FSR, as long the conditions noted below are satisfied). Assuming the input power, the reflection and transmission coefficients, and the intrinsic loss all to be independent of frequency over this interval, the integrated drop fraction D_I, the fraction of the incident power in the integration interval that is transmitted out the drop port, is given by

$$D_I = \frac{D_0}{\sqrt{1 + \left(\frac{4}{\Delta\delta}\right)^2}} \rightarrow \begin{cases} D_0 = 4T^2/(\Delta\delta)^2 & \text{for } \Delta\delta \gg 1 \\ D_0\Delta\delta/4 = T^2/\Delta\delta & \text{for } \Delta\delta \ll 1 \end{cases}. \quad (5.8)$$

The spectrometer signal will be proportional to this integrated fraction times the incident power in the detection interval. Note the functional dependence of the detected signal on the linewidth (or total loss) $\Delta\delta = 2T + \alpha L$ in the two limiting cases of large and small linewidth. The first limiting case says that when the linewidth fills the integration interval, the drop fraction equals what would be found by using a single-frequency source tuned to WGM resonance; this holds for either low Q or many overlapping modes in the integration interval, so that integration introduces no additional linewidth dependence. The second limiting case is the usual one for well-separated modes, and is the same as what results from

approximating each WGM's narrow transmitted lineshape as a Lorentzian; this holds as long as the integration interval is wide compared to the WGM linewidth.

Let the effective loss coefficient now include, in addition to intrinsic loss, a contribution due to absorption (and scattering) by the analyte contained in the evanescent fraction f of the WGM: $\alpha = \alpha_i + f\alpha_a$. The effect of the analyte on the resonant (single-frequency) drop signal D_{0a}, when analyte absorption is a small fraction of the total loss, can be written in terms of an approximate effective absorption path length L_{eff} as defined below:

$$D_{0a} = \frac{4T^2}{\left(2T + \alpha_i L + f\alpha_a L\right)^2} = \frac{D_0}{\left(1 + \frac{1}{2}\alpha_a L_{eff}\right)^2}, \quad \text{where } L_{eff} = \frac{2fL}{2T + \alpha_i L}. \quad (5.9)$$

Here, L_{eff} is the effective absorption path length as defined in the low-analyte-absorption limit. However, the last expression for D_{0a} is valid even for large analyte absorption, that is, there are no restrictions on the size of $\alpha_a L_{eff}$ as long as $f\alpha_a L \ll 1$.

Then, for broadband input, the integrated drop fraction in the presence of analyte, D_{Ia}, will also be given by (5.9) in the large linewidth limit. For precessing-mode drop-port output collected without being spatially filtered by an aperture[15], this limit applies for the following reason. The incident focused light (Fig. 5.2) incorporates a bundle of wavevectors and so excites precessing modes over a range of angles with respect to the equatorial plane. The round-trip distance depends on this angle in a spheroid, so the precessing modes are frequency shifted by amounts depending on angle. The result is many modes (not only a range of different angles, but also ranges of different radial orders and different polar orders) that overlap to fill the integration interval, so when the analyte absorption broadens the linewidth and reduces the transmission of each mode, the broadening is not noticed, because the integration interval remains filled. Thus only the decrease in amplitude is observed, just as in the single-frequency resonant case. The overlapping of modes also means that the exact value of the spectrometer resolution interval does not matter. This large-linewidth-limit functional dependence of the integrated drop signal on $\alpha_a L_{eff}$ as given in (5.9) has been tested in recent experimental work[15], described briefly below in Sect. 5.4.

5.3   Microcavity-Enhanced Detection of Atmospheric Trace Gases

So far, in label-free chemical sensing applications, the interaction of a WGM's evanescent component with an analyte in the ambient or adsorbed on the micro-resonator's surface has led to the development of two sensing methods. These are monitoring of the WGM resonance frequency shift due to the analyte's change of

the effective index of refraction[6,7] and measurement of the amount of Q spoiling (increase in WGM linewidth) resulting from analyte absorption[8].

Another method that we introduced earlier[16] and described in Sect. 5.2 is based on recording changes in the resonant dip depth observed in the coupling-fiber throughput[10]. In this implementation[4], we use a cylindrical microcavity in which a WGM is excited around its circumference using an adiabatically tapered fiber tangentially in contact with the cylinder. Tunable diode laser (TDL) light is injected at one end of the tapered fiber and the throughput at the other end displays a Lorentzian dip every time a WGM resonance is excited. The analysis of such an efficiently coupled microcavity is well known[10–13]. Absorption by a molecular trace gas in the air surrounding the microresonator will change the depth of a resonant dip, and this change is what we measure[3] This method enables TDL absorption spectroscopy experiments in which the long effective absorption path lengths that result are confined within less than a cubic millimeter.

Although the cylindrical microresonators provide a lower sensitivity than the microspheroids that we used earlier[16] (however, see further discussion in Sect. 5.3.3), they offer some very attractive advantages. First, they are far easier to mount in a strain tuner, and are much less susceptible to mechanical failure than microspheroids tuned by compression. Second, alignment is easier since there is only one degree of freedom to adjust (making the taper perpendicular to the cylinder axis) vs. two for the spheroids. Third, the mode spectrum is sparser, making locking of a WGM to the laser easier. And, finally, because the microcylinder is just a standard optical fiber, different resonators are nearly identical in diameter, providing better repeatability of results.

For chemical sensing applications, we model the microresonator as described in Sect. 5.2.1, and monitor the depth of a resonant dip in the fiber throughput. This dip depth is given by (5.3). As described in Sect. 5.2.1, absorption by the analyte causes a small change in dip depth that is proportional to the analyte absorption coefficient[3], as in (5.4). When a WGM is frequency locked[17] to the input laser, the WGM stays on resonance with the laser and, as the laser scans in frequency, the throughput of the bitapered fiber displays the locus of the bottom of the WGM resonance dip as it follows the laser scan. When an absorption line of the surrounding gas is present within the scan, there is a change in the WGM dip depth that traces the contour of the respective absorption line. Since in such a setup the microresonator is always on resonance, light interacting with the gas executes many round trips around the circumference, resulting in a long effective interaction path length.

The theoretical effective absorption path length was given in (5.5); the experimental effective absorption path length takes the form shown in (5.6) and is found by measuring the dip depth in the absence of analyte (M_0) and in the presence of analyte ($M_0 + \Delta M_0$). Equation (5.6) thus provides a way to express the relative sensitivity (fractional change in dip depth) of the WGM gas sensor based on the experimental effective absorption path length, the length of a hypothetical absorption cell that has the same sensitivity. The model is tested by comparing experimental and theoretical effective path lengths.
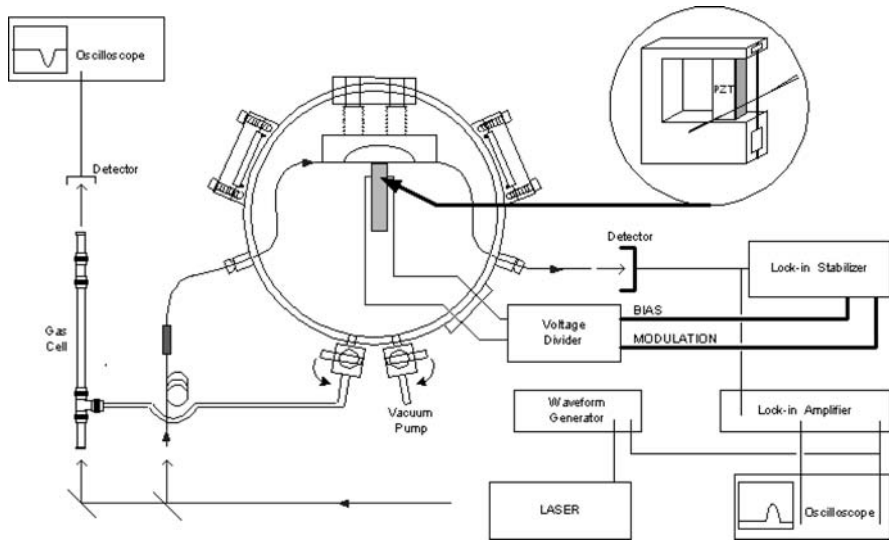
Fig. 5.3 Experimental setup. Light from a frequency-scanned cw diode laser is launched into a bitapered fiber to excite WGMs of the microresonator. The microresonator is held in a PZT fixture for tuning and locking purposes (*inset*). Reprinted from Ref. 4 with permission. © 2008 Optical Society of America

5.3.1 Experimental Setup

Figure 5.3 shows the experimental setup[4]. A cylindrical vacuum chamber with a transparent top plate and side windows for viewing the optical setup is connected to a reference cell that is used for calibration. The gas mixes and pressures in the chamber and cell can be varied independently. Typically, a low partial pressure of the molecular gas of interest is added to air at atmospheric pressure in the main chamber. Light from a cw TDL is coupled into the reference cell and into a single-mode optical fiber. The fiber passes through a polarization controller that is adjusted to ensure that WGMs of a single polarization (TE or TM) are excited. Then the fiber is fed into the vacuum chamber where its adiabatic bitaper is brought into contact with the microresonator. The position and the orientation of the coupling fiber are controlled, via bellows-sealed feedthroughs, by a positioner located outside the chamber. The 125-μm-diameter cylindrical fused-silica microresonator is mounted in a fixture (inset, Fig. 5.3) that allows tuning of the WGMs by stretching the resonator when a voltage is applied to the piezoelectric transducer (PZT). The microcylinder is just a standard optical fiber whose jacket has been softened by soaking in acetone and then pulled off. The fiber is then soaked in clean acetone and wiped with lens paper and methanol. This preserves the optical quality of the microresonator's surface. After the coupling fiber exits the chamber, its output is collected onto a detector. The signal from the detector is split, part of it being fed into a lock-in stabilizer in order to lock individual WGMs to the laser.

   The locking is done as follows[17]. A WGM is tuned to be in resonance with the
TDL by adjusting the PZT bias voltage, and the lock-in stabilizer is switched on.
The lock-in stabilizer applies a 518-Hz dither voltage to the PZT and peak-locks the
WGM to the laser. Then as the laser scans in frequency the lock-in stabilizer tunes
the dc bias voltage on the PZT, maintaining the WGM on resonance with the laser
over the entire scan range. When locked, the maximum excursion from true
resonance is less than 5% of the WGM's linewidth. This tuning jitter results in
unfiltered noise on the signal that is less than 1% of the dip depth.

   The rest of the detector signal is noise filtered and amplified by a lock-in
amplifier. The output of the lock-in amplifier is monitored by an oscilloscope,
and recorded as the laser scans across the gas's absorption line. The result is a
spectral profile of the gas absorption, impressed on the depth of the locked resonance
dip. This is then analyzed using (5.6) to find an experimental effective absorption
path length.

5.3.2   Results

Experimental results are reported here for a few trace gases, having absorption
features in the vicinity of 1.65 μm, in air at atmospheric pressure. The gases
investigated were methane (CH_4)[18,19], methyl chloride (CH_3Cl)[18], and ethylene
(C_2H_4)[19]. The transitions involved belong to overtone and combination bands
involving the C-H bonds. For example, the absorption lines of methane in
this wavelength range correspond to the C-H asymmetric stretch vibrational over-
tone $2v_3$[18–20]. There are three lines of approximately equal strength that are roughly
equally spaced at intervals of about 400 MHz and pressure broadened by air to about
4 GHz each[20]. The methyl chloride lines probably belong to the perpendicular
component of the $2v_4$ band[18]; however, the assignment for ethylene is less certain[19].

   These results are presented in Fig. 5.4 and the details are summarized in
Table 5.1. For each gas in Fig. 5.4, the dip-depth variation (change in M_0, at 50×
amplification) shows the detected absorption profile. These are not to scale, in the
sense that the full dip is far too large to show at this amplification. Straight lines are
added to make the variation clear; the slope of these lines (again, amplified 50×)
may be an effect of the differential tuning of adjacent WGMs resulting in slightly
varying mode overlap, because there is no variation in coupling (or in x) over the
10-GHz frequency scan range. When the gas compositions and pressures are the
same in the test chamber and in the reference cell, both give the same lineshape. For
example, the top traces in Fig. 5.4 (methane) can be fitted well by a sum of three
unresolved Lorentzians.

   In Table 5.1, the theoretical effective absorption path length is calculated from (5.5)
using, for example, in the case of methane, $x = 0.28$ (calculated from the dip
depth M_0; the dip gets shallower with analyte absorption, so the WGM is under-
coupled), $f = 1.6\%$ (estimated from a computation of the field distributions at the
same wavelength in a microsphere of the same diameter), and $\alpha_i = 0.0061 \text{ cm}^{-1}$
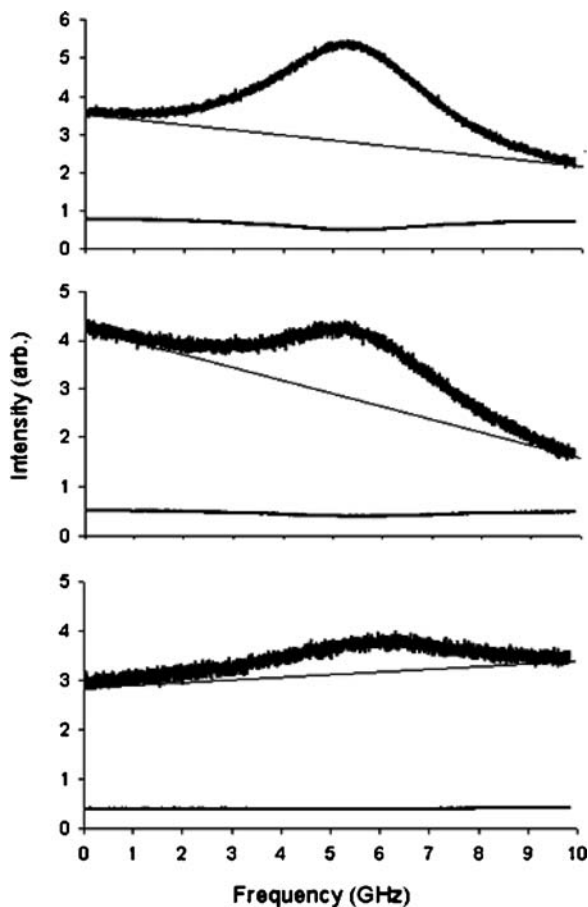
Fig. 5.4 From top down: the measured absorption profiles of methane, methyl chloride, and ethylene obtained using a WGM locked to the laser. In each case, the top trace shows the amplified variation in dip depth and the bottom trace is the transmission profile of the gas in a 16-cm absorption cell. The frequency axis shows the tuning range. Reprinted from Ref. 4 with permission. © 2008 Optical Society of America

Table 5.1 Summary of results from Fig. 4, for gases in air at atmospheric pressure. Reprinted from Ref. 4 with permission. © 2008 Optical Society of America

Gas	L_{eff}^t (mm)	L_{eff}^e (mm)	WGM Q	λ (nm)	Partial pressure (atm)
CH_4	15.0 ± 3.0	17.7 ± 1.7	7×10^6	1,653.722	0.01
CH_3Cl	7.2 ± 1.5	6.3 ± 1.1	3×10^6	1,651.59	0.01
C_2H_4	13.6 ± 2.7	13.2 ± 2.6	5×10^6	1,654.23	0.02

(found from the values of Q and x). The experimental effective absorption path length was obtained using (5.6) in which, again for methane, $M_0 = 68.4\%$ and $\Delta M_0 = -0.7\%$. The value of the methane absorption coefficient that was used for this

concentration, $\alpha_a = 0.0058$ cm^{-1}, was extracted from the reference cell transmission measurements, and is in reasonable agreement with the value expected from parameters found in the HITRAN database[20]. Similar calculations were done for the other gases.

For each trace gas in Table 5.1, there is good agreement between the theoretical and the experimental effective absorption path lengths. For the theoretical values, the main source of error is in calculating the evanescent fraction, because it takes on different values for different modes, and the WGM that is used is not definitively identified. Uncertainty in the measured value of α_a and the residual noise on the traces corresponding to the locked WGMs are responsible for the error in determining the experimental effective absorption path length.

5.3.3   Summary

Cavity-enhanced laser absorption spectroscopy using microresonator WGMs has been demonstrated by locking the WGM resonances to the laser. Atmospheric trace gases in the evanescent fraction of the locked WGM are detected. The gas molecules remain in the ambient air and are not adsorbed onto the microresonator surface. The relative detection sensitivity is characterized by an effective absorption path length, and its experimentally determined value is in good agreement with the theoretical prediction. The major advantages of our setup are miniaturization and relatively low cost. Although the detection volume is less than a cubic millimeter, relatively large effective absorption path lengths on the order of centimeters are obtained.

From Fig. 5.4, the detection limit can be estimated to be about one-tenth of the concentrations shown or about 1,000 parts per million. This is an order of magnitude higher than that estimated for a microsphere in Ref. 16, because the Q is lower by a factor of $20 - 5 \times 10^6$ vs. 10^8. The other advantages of the microcylinder mentioned in the introduction to this section outweigh this sensitivity deficit and, in addition, we now have very good agreement with theory. Nevertheless, other microresonator geometries can also be envisioned for enhancing the sensitivity of the setup. Using a fiber fusion splicer, for example, a microspheroidal resonator with two stems can be obtained. Mounting it into the same PZT device would enable tuning of the WGMs in the same fashion as the microcylinder[21]. However, the curved surfaces of the microspheroid should, in principle, result in higher-Q WGMs with greater detection sensitivities, i.e., longer effective absorption path lengths.

5.4   Extensions of Method and Further Enhancements

The cavity-enhanced evanescent-wave sensing method described in Sect. 5.2 and applied to gases in Sect. 5.3 can also be employed for the detection of chemicals in liquid solution. In addition, the intracavity enhancement provided by the high-Q

microresonator can be further enhanced by other techniques, thereby increasing the sensitivity. Some of these extensions and enhancements are briefly described in this section.

5.4.1 Sensing in Liquids: Laser and Broadband

Both the modes of operation described in Sect. 5.2 may be used for the detection of chemicals in liquid solution. Because the analyte's absorption linewidth is very broad, overlapping several (or many) WGMs, no tuning of the microresonator, or locking of a WGM to the scanning laser is necessary. In fact, a broadband source such as a light-emitting diode (LED) may be used.

Microcavity-enhanced absorption sensing experiments were performed on two dyes dissolved in methanol, using a cw tunable Ti:sapphire laser at 800 nm and a TDL at 1,550 nm[22]. In both cases, the experimental sensitivity was such that 100-pM changes in concentration could be detected. This is especially remarkable at the longer wavelength, because at 1,550 nm methanol is strongly absorbing, with an absorption coefficient of about 8.8 cm^{-1}. This provides further confirmation of the theory of Sect. 5.2.1[3]. However, the experimental sensitivities are approximately two orders of magnitude greater than predicted by the theory. This might be a result of adsorption of dye molecules onto the surface of the microresonator, which could be tested by using certain surface treatments. Another possible explanation is multiple-fiber-mode excitation, described in Sect. 5.4.2.

The second implementation, described in Sect. 5.2.2, uses a broadband source and spectral detection, using a spectrometer with resolution of the order of the resonator's FSR (the FSR is about 200 GHz for a 330-μm diameter microsphere, or 0.2 nm for wavelengths around 550 nm). Precessing modes in a microsphere are employed to give a drop spectrum that is modified by analyte absorption. In this case, the total loss determines the sensitivity, but with prism coupling it is more likely that the system will be in the undercoupled limit. The setup shown in Fig. 5.2 has been used for the detection of Lissamine Green B dye in pH 5 citrate buffer using a 635-nm LED light source[15]. Effective path lengths of about 1 cm were observed, and the behavior of the drop signal as a function of concentration (hence α_a) was in most cases exactly as predicted by (5.9).

5.4.2 Prospective Methods for Sensing Enhancement

Two methods of further enhancing detection sensitivity rely on the use of multiple resonators or multiple fiber modes. The first will just be mentioned briefly, because although it is absorption based it uses a frequency shift. When two microresonators have resonances that are coincident in frequency, and the second resonator is brought near to the first resonator, which is in contact with the coupling fiber, the

coupling between resonators will split the mode and produce the analog of electromagnetically induced transparency. This coupled-resonator-induced transparency (CRIT) response[23] is sensitive to absorption in the ambient, and the presence of absorbing molecules will cause the frequency splitting to change[24]. This provides another sensing method that is enhanced by the CRIT response and benefits from the fact that the splitting is independent of any overall frequency shift.

The second enhancement method involves multimode excitation of a single WGM. If one uses a tapered coupling fiber whose taper-down transition is nonadiabatic, but whose taper-up transition is adiabatic, then as light propagates from the single-mode untapered fiber, where it is core guided, into the taper waist region, where it is cladding guided, higher-order fiber modes can be excited, most likely the HE_{12} mode in addition to the fundamental HE_{11}. These modes have the same frequency but different propagation constants. They couple to the same WGM, but their relative input phase will depend on the position of the microresonator along the taper waist region. Light will couple out of the WGM back into the taper modes, but only the HE_{11} will then couple into the core-guided mode of the untapered fiber for detection, because the second taper transition is adiabatic. For the proper combination of relative phases and coupling strengths, we have shown that the absorption sensitivity can be enhanced by about two orders of magnitude over the usual single-fiber-mode case. The throughput dip depth is no longer a good indicator of intracavity power, and thus a small change in effective intrinsic loss can make a large change in the dip signal. It may be that the experimental disagreement from theory for liquid sensing in Sect. 5.4.1 is a result of this multiple-fiber-mode coupling effect.

5.4.3 Gold-Nanorod-Enhanced Sensing

We have developed a technique for growing gold nanorods directly on the surface of a microresonator, using semiconductor (HgTe) nanoparticles as seeds[25]. This method has proven to give a better nanorod yield than the use of gold nanoparticle seeds. When the nanorods have an aspect ratio (length to width) of about 5 or more, their longitudinal surface plasmon resonance is shifted from the visible into the infrared ($\sim$800 nm). This enhances the coupling of light from a tapered fiber into WGMs[26,27]. The strong surface field enhancement provided by the longitudinal plasmon resonance effectively increases the strength of the WGM's evanescent component, giving a large increase in fiber-microsphere coupling; the strength of this coupling is measured by the probability of tunneling into the WGM experienced by a photon as it travels down the fiber past the sphere. Remarkably, the coupling can be increased by a factor that is typically between 100 and 1,000, while the intrinsic loss (surface scattering) increases by less than a factor of three.

The enhanced evanescent field, as confirmed by the coupling enhancement results noted above, has been shown to significantly enhance detection sensitivity in preliminary experiments using dye in water solution at 800 nm. In addition, a

nanorod-coated microresonator can be used for surface-enhanced Raman scattering (SERS). SERS greatly increases the number of molecular species that can be detected, because the molecule no longer has to be resonant with the driving laser.

5.4.4 Summary

The enhancement techniques briefly described in this section are just a few of those that can be used to make cavity-enhanced evanescent-wave chemical detection even more sensitive. The use of dielectric microresonators with tapered-fiber coupling enables performance that is difficult to achieve in other configurations, while minimizing the sensor size.

5.5 Surface and Thin-Film Characterization

It is well known that the WGMs of dielectric microresonators can serve as sensitive probes of their environment, through the environment's interaction with the WGMs' evanescent components. In addition to microcavity-enhanced laser absorption spectroscopy of molecules in the ambient gas or liquid, another effect that can be used as an environmental probe is the temperature sensitivity of WGM resonance frequencies[28–30]. A high-Q microresonator can easily measure mK temperature changes; while this can be a complication for some applications, it can also be put to use in detecting heat absorbed and heat lost by the microresonator. At wavelengths around 1,570 nm, the resonance frequency will shift down by approximately 1.6 GHz for each Kelvin increase in temperature, due primarily to the change in refractive index[31], to which is added the effect of thermal expansion.

The experiments reported here are extensions of some of our earlier work[32]. First, a microsphere is heated by focusing a laser beam onto it; upon turnoff of the heating beam, the microsphere relaxes back to room temperature. From its relaxation rate, observed via the WGM frequency shift using a weak TDL, we can calculate the thermal conductivity of the surrounding air. Doing this for a range of pressures allows us to determine the thermal accommodation coefficient of air on the surface (roughly the probability that a gas molecule will equilibrate with the surface after one collision). The surface in these experiments is either bare fused silica or a polymer film coating. This is a novel method for measuring accommodation coefficients. In a second experiment, use of the diode laser at higher power (without an external heating beam) produces thermal bistability; since the experiment with external heating determined the heat loss, the bistable response gives us the heat supplied by the fraction of total optical power lost due to absorption. This absorption results primarily from a water layer on the surface of a bare sphere, and for a coated sphere it is due to the polymer film. The precision of these
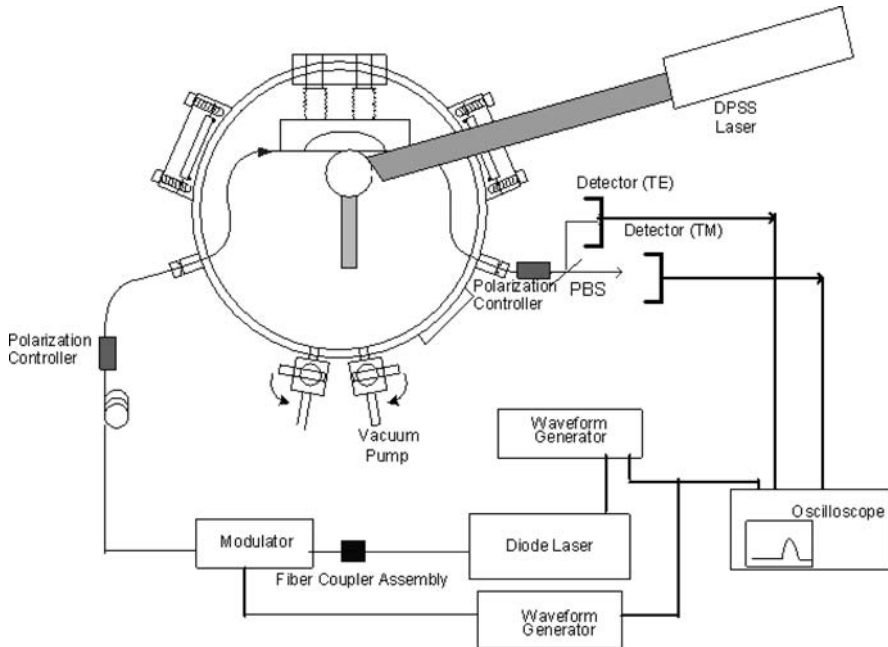
Fig. 5.5 Experimental setup. The diode laser is frequency scanned by one waveform generator, while the other controls the modulation. The light couples from a tapered fiber into and back out of microsphere WGMs, and the throughput is detected. A polarizing beamsplitter (PBS) separates throughput of the two polarizations. A diode-pumped solid-state laser can be used as an external heat source for the microsphere, and the vacuum chamber allows control over the ambient pressure. Reprinted from Ref. 5 with permission. © 2008 International Society for Optical Engineering

measurements is quite good (∼5%), so the prospect of using these techniques for thin-film characterization is promising.

5.5.1 Experiments

The experimental setup is shown in Fig. 5.5. The microsphere is mounted in a cylindrical vacuum chamber that has a transparent top plate and side windows for viewing. The pressure in the chamber can be varied from above atmospheric to about 2 mTorr. Light from a cw TDL is coupled into a modulator, from which it exits into a single-mode optical fiber that passes through a polarization controller before being fed into the chamber, where its adiabatic bitapered region is brought into contact with the microsphere. The position and orientation of the coupling fiber are controlled, via bellows-sealed feedthroughs, by a positioner located outside the chamber. The polarization controller is adjusted to ensure that WGMs of a single polarization (TE or TM) are excited, and after the fiber is fed out of the chamber the

two polarizations in the throughput can be detected separately. The modulator is normally off, but can be turned on to provide a square-wave intensity modulation; the throughput response to the square-wave input tells us whether a WGM is undercoupled or overcoupled (intrinsic or coupling loss dominant, respectively) without changing the geometry of the system. The microsphere is actually a prolate spheroid of average radius about 300 μm, fabricated from optical fiber in such a way as to have very thin stems both above and below. The double stem helps to make the mounting more rigid, since the stems are so thin (tapering to just a few μm). The 532-nm heating beam of about 1 W comes from a frequency-doubled Nd:YVO$_4$ laser, and is focused through a side window onto the microsphere.

The diode laser is scanned up and down in frequency by a triangle wave, so that the scan should be linear in time and have the same rate in both directions. In the thermal accommodation coefficient experiments, the external beam heats the microsphere to a few K above room temperature and is then turned off. The diode laser is kept at fairly low power ($\sim$7 μW) so that it does not appreciably heat the microsphere. Displacement of a WGM's throughput dip from one scan trace to the next is analyzed to find the relaxation time constant as the microsphere returns to room temperature. Results from the two scan directions are averaged to reduce error due to residual scan nonlinearity. This is done over a wide range of pressures (about four orders of magnitude). The time constant provides the measured thermal conductivity of the surrounding air, and fitting the thermal conductivity vs. pressure curve determines the thermal accommodation coefficient, as described in Sect. 5.5.2.

The thermal bistability experiments use the same system, minus the external heating laser. Now the diode laser power incident on the microsphere is on the order of 150 μW, so that the diode laser will heat the microsphere if it is scanned slowly enough across a WGM resonance. Since the relaxation time constant is known from the previous experiment, fitting the bistable throughput trace to a simple model will determine the single free parameter, which is the fraction of the total power loss that is due to absorption (assuming the absorbed power is converted to heat rather than reradiated). This is described in Sect. 5.5.3. Because the absorption in fused silica is so low in this wavelength range, we assume that all the absorption takes place in the water layer on the surface of the bare sphere or in the polymer layer on the coated sphere. Then from the known absorption coefficient for bulk water, we can estimate the thickness of the water layer. Likewise, knowing the thickness of the polymer film, we can find its absorption coefficient.

5.5.2 Accommodation Coefficients

Analysis of these experiments is simplified by the fact that the thermal conductivity of fused silica is much greater than that of air. Therefore, the microsphere can be treated as being in thermal equilibrium (uniform internal temperature distribution) at all times because of its very fast internal relaxation[33]. We assume that heat loss through the stems is negligible because of their small masses and long conduction

paths. Because the microsphere is so small, convection is negligible[34], and so heat loss occurs through conduction by the surrounding air and by radiation. Define T to be the deviation of the microsphere's temperature above room temperature T_R (in this section, T_c will be used to denote coupling loss), and the relaxation equation can be written as follows for $T \ll T_R$:

$$\frac{dT}{dt} = -\frac{1}{mc}\left(4\pi a k_{air} + 16\pi a^2 \varepsilon \sigma T_R^3\right)T = -\frac{1}{\tau}T, \tag{5.10}$$

where m is the microsphere's mass, c is the specific heat of fused silica, a is the microsphere's radius, k_{air} is the measured thermal conductivity of air, ε is the emissivity of fused silica, σ is the Stefan–Boltzmann constant, and τ is the thermal relaxation time constant. Because the temperature variation is small, any temperature dependence of these parameters can be neglected. However, k_{air} will depend on pressure; the measured value will begin to decrease as the molecular mean free path becomes comparable to the size of the microsphere. The pressures used are such that our data are predominantly in the slip-flow or temperature-jump regime,[35] that is, the pressure is higher than the free-molecular-flow regime. This means that the pressure dependence of k_{air} is given by

$$k_{air}(p) = \frac{k_{atm}}{1 + \left(\dfrac{2-\alpha}{\alpha}\right)\dfrac{k_{atm}\sqrt{2\pi R T_R}}{(c_p + c_v)pa}}. \tag{5.11}$$
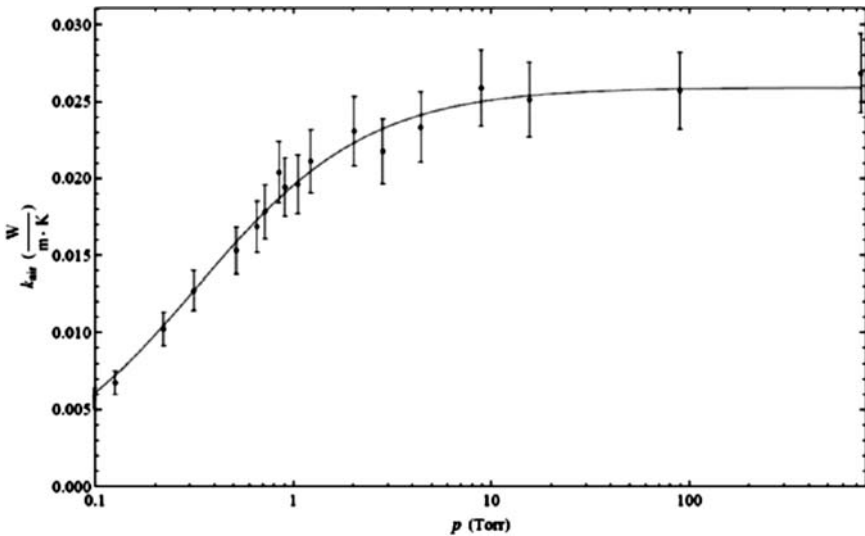

Fig. 5.6 Pressure dependence of thermal conductivity of air, measured using a PDDA-coated microsphere of effective radius 298 μm. The fit to (5.11), shown as the *curve*, gives a thermal accommodation coefficient of 0.92 for air on PDDA. Reprinted from Ref. 5 with permission. © 2008 International Society for Optical Engineering

In (5.11), k_{atm} is the thermal conductivity of air at atmospheric pressure; R is the gas constant per unit mass of air; c_{p} and c_{v} are the heat capacities of air at constant pressure and volume, respectively; p is the air pressure; and α is the thermal accommodation coefficient for air on the surface of interest. Fitting a plot of k_{air} vs. p then determines the value of α, the single free parameter.

Experimental values for k_{air} vs. p were found for two fused-silica microspheres, one bare and the other coated with a polyelectrolyte layer (Fig. 5.6). The second microsphere was dipped in a 0.5% solution of poly(dimethyldiallylammonium) chloride (PDDA) for about 30 min to produce a polyelectrolyte surface layer approximately 1-nm thick[36]. Because the microresonators were so prolate, an effective radius was chosen that gave the best fit of (5.11) to the data. For example, the bare sphere had a minor radius of 295 μm, a major radius of 375 μm, and an effective radius of $a = 325$ μm. Similarly, the PDDA-coated sphere had an effective radius of $a = 298$ μm. For the accommodation coefficient of air on fused silica, we find $\alpha = 0.84 \pm 0.03$, in good agreement with previous measurements for nitrogen and oxygen on glass[37]. Our value found for the accommodation coefficient of air on PDDA is $\alpha = 0.92 \pm 0.03$, slightly larger than on fused silica, as might be expected from the more porous structure of the PDDA surface.

For the PDDA-coated sphere, since the coating thickness is much less than the effective radius, we use the specific heat of fused silica in (5.10). The emissivity of PDDA is not known, so the value for fused silica was used ($\varepsilon = 0.87$); the results are not sensitive to the exact value, because the radiation loss is smaller than the heat loss by conduction. Looking at the data in Fig. 5.6, no obvious effect of heat loss from the stems is seen. If stem loss were significant, the measured value of k_{air} would begin to fall off at a higher pressure than it does. Perhaps, however, the somewhat larger scatter and error in the data at high pressures may be a consequence of some stem loss, as well as residual heating by the diode laser. The fit of (5.11) to the data is quite sensitive to the value of α, so its error is only on the order of 3% despite the larger errors in k_{air}. The fit remains good even to the lowest pressures of 0.1 Torr, indicating that the transition to free-molecule behavior has not yet been seen. At even lower pressures, estimated for these spheres to be on the order of 10 mTorr[35], the data points should begin to fall below the curve of (5.11). This appears to be an entirely new method for measuring the accommodation coefficient; nothing similar is mentioned in the literature[37].

5.5.3 Thermal Bistability

In these experiments, power absorbed from the WGM-exciting diode laser, operating at higher power, heats the sphere. The laser is scanned slowly in frequency across a resonance. The scan rate is slow enough that the assumption of internal thermal equilibrium in the microsphere holds, except perhaps during the fast throughput power jumps (see Figs. 5.7 and 5.8). In equilibrium, the power absorbed depends

on the detuning from the temperature-dependent resonance, the depth of the resonance dip, and the incident power. Thus a heating term can be added to the right-hand side of (5.10) to describe the microsphere's temperature as a function of time[32]:

$$\frac{dT}{dt} = \frac{\beta M_0 P_{\text{inc}}}{mc} \frac{\left(\frac{\Delta v}{2}\right)^2}{(v(t) - v_0 + bT)^2 + \left(\frac{\Delta v}{2}\right)^2} - \frac{T}{\tau}, \tag{5.12}$$

where M_0 is the fractional dip depth[3], P_{inc} is the incident power (equal to throughput power when off resonance), Δv is the linewidth of the Lorentzian WGM at $v_0 - bT$ where b is the 1.6 GHz K^{-1} temperature shift, and the only free parameter, β, is the fraction of the total power loss ($M_0 P_{\text{inc}}$) that is due to absorption. Fitting a throughput trace to a tuning curve derived from (5.12) gives the value of β. Now from (5.3), where the loss ratio is $x = T_c/2\pi a \alpha_i$, and the measured (loaded) quality factor

$$Q = \frac{v_0}{\Delta v} = \frac{2\pi n}{\lambda(1 + x)\alpha_i}, \tag{5.13}$$

where n is the index of refraction of fused silica and λ is the wavelength, the intrinsic loss coefficient α_i can be found. There are two solutions, corresponding to the undercoupled ($x < 1$) and overcoupled ($x > 1$) cases, which is why the modulator is needed in the experiment to determine the coupling regime. Then the effective absorption coefficient is $\alpha_{\text{abs}} = \beta \alpha_i$. An approximate expression for the relation between the effective absorption coefficient of the water layer or thin film, of thickness δ, and its bulk absorption coefficient α_b has been given[38]:

$$\delta \cong \left(\frac{\lambda a}{\pi n^5}\right)^{1/2} \frac{\alpha_{\text{abs}}}{4\alpha_b}. \tag{5.14}$$

Using (5.14) and the determined value of α_{abs}, we can estimate δ if α_b is known, and vice versa. Two examples of thermal bistability data, fit to a calculated tuning curve based on (5.12), are shown below. Figure 5.7 is for the bare sphere, and Fig. 5.8 is for the PDDA-coated sphere. In the figures, the laser scans slowly across a TM-polarized WGM dip (taking several thermal relaxation times to scan Δv), first down in frequency, then reversing at the vertical dashed line, and scanning back up in frequency across the same mode. The continuous smooth lines are the theoretical fits.

The fitting to the data in Figs. 5.7 and 5.8 gives the values of α_{abs} to about 5% precision. The value found for the bare sphere is consistent with the values found at other pressures and for overcoupled modes. Using (5.14) and the known bulk absorption coefficient of water (at these wavelengths, water has $\alpha_b \approx 800$ m^{-1})[14] we estimate $\delta \approx 6.7$ pm from Fig. 5.7. This corresponds to water coverage on the
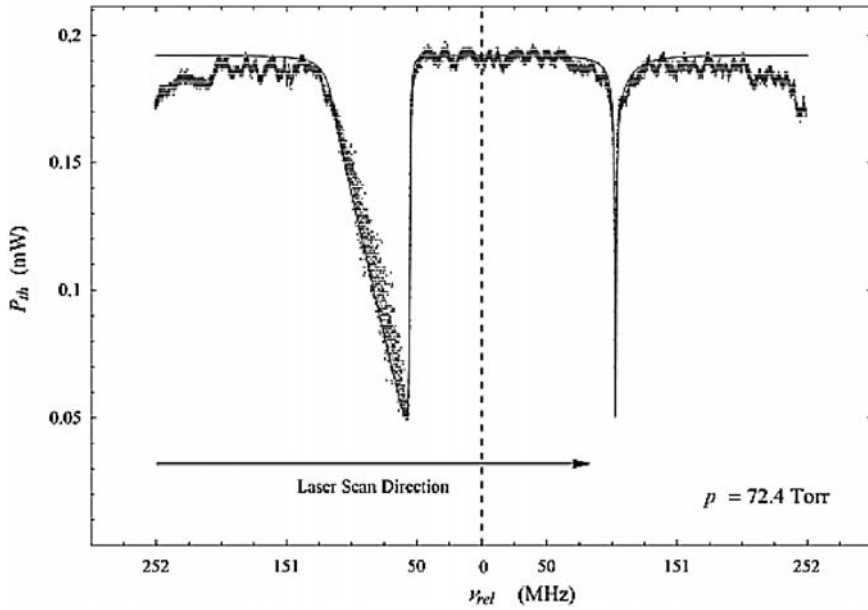
Fig. 5.7 WGM resonance dip showing thermal bistability. For this undercoupled mode in the bare sphere with $Q = 3.14 \times 10^7$, the fit gives $\alpha_{abs} = 0.00419 \text{ m}^{-1}$. Reprinted from Ref. 5 with permission. © 2008 International Society for Optical Engineering
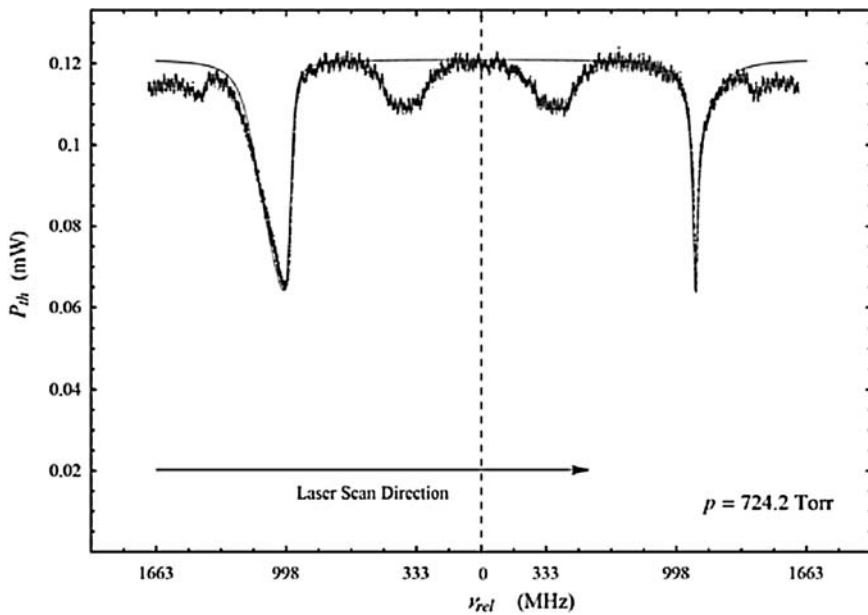

Fig. 5.8 WGM resonance dip showing thermal bistability. For this undercoupled mode in the PDDA-coated sphere with $Q = 2.25 \times 10^6$, the fit gives $\alpha_{abs} = 0.428 \text{ m}^{-1}$. Reprinted from Ref. 5 with permission. © 2008 International Society for Optical Engineering

fused-silica surface of about 5–6% of a monolayer. A typical value is about one monolayer; our values may be lower than this because the sphere had been held at a low pressure for some time before the measurements were made. Applying the same analysis to Fig. 5.8, we estimate $\delta \approx 0.66$ nm. This value indicates that the absorption coefficient of the PDDA film is of the same order of magnitude as that of bulk water.

5.5.4   Summary

The temperature sensitivity of the resonant frequencies of WGMs in a microsphere has been employed to measure the thermal conductivity of the ambient air as a function of pressure, and these results have enabled a quantitative explanation of thermal optical bistability observed in the microsphere under conditions of larger incident power. Measuring the thermal relaxation time to determine k_{air} vs. p, and fitting the results to the temperature-jump model of (5.11), determines the value of the thermal accommodation coefficient of air on the microsphere surface. Since these measurements can easily be done with various gases, using different surface coatings (thin compared to the wavelength), a large number of gas-surface interactions can be studied. This optical technique using microresonators is very well suited to making these measurements, and so adds a new method for the study of the interaction of gases with surfaces.

Measuring thermal bistability and fitting the observed mode profiles to the model, combined with the intensity modulation that permits determining the coupling regime without having to move any part of the setup, allow us to characterize the system losses. The coupling loss and intrinsic loss can be determined separately, and the intrinsic loss separated into its scattering and absorption components[39]. The absorption component is predominantly due to the surface water layer on a bare sphere, or to the coating on a sphere to which a thin film has been applied. This technique then also permits the measurement of the absorption coefficient of the film, and it can be applied to films of any refractive index and absorption coefficient, provided only that the film is thin enough.

5.6   Conclusions

The methods and results presented in this chapter describe the utility of chemical sensing techniques based on microcavity-enhanced optical absorption. In Sect. 5.2, a theoretical analysis was given for both tunable single-frequency operation and broadband operation. Using a single tunable frequency and measuring the effect of analyte absorption on the depth of the throughput dip was shown to give better relative sensitivity in some cases than methods such as frequency shift or cavity ringdown. It was further shown that this method makes it possible to measure weak

analyte absorption against the background of a strong solvent absorption. It was also shown that using a broadband source and spectral detection of the drop-port output gives nearly as great a sensitivity as the tunable single-frequency method. For both methods, it was shown how experimental results can be easily compared to the theory.

The tunable single-frequency method was used, with the added modification of locking the WGM to the laser, for the detection of atmospheric trace gases. In this case, good agreement was found between experiment and theory. The low-Q cylindrical microresonators used in Sect. 5.3 provide centimeter effective absorption path lengths, but high-Q microspheres used in similar experiments have given effective path lengths as large as 10 m[32]. Tunable single-frequency sensing experiments in liquids, described in Sect. 5.4.1, have confirmed the ability to detect an analyte in a strongly absorbing solvent. In liquids, effective path lengths of several meters were found; this is nearly two orders of magnitude greater than the theoretical expectation, perhaps because of an inadvertent enhancement by one of the methods mentioned in Sect. 5.4.2. There are several ways to further enhance the sensitivity of microcavity-enhanced absorption sensing, and some of these will be quite easy to implement, such as growing a sparse distribution of gold nanorods on the microresonator surface.

The broadband analysis was confirmed by the experimental results mentioned in Sect. 5.4.1. This method can also be further enhanced by some of the techniques described in Sects. 5.4.2 and 5.4.3. The conclusion is that these methods of microcavity-enhanced optical absorption sensing provide compact, inexpensive, and sensitive detectors for molecular species in the ambient gas or liquid, and that further increases in sensitivity can be implemented to make them even more competitive. The molecular-transition specificity that is implicit in absorption spectroscopy is a limiting restriction, but the surface-enhanced Raman sensing that is enabled by metallic nanoparticles on the microresonator surface can significantly increase the number of molecular species that could be detected.

The sensing methods summarized thus far are intended for absorption detection of molecules in the ambient, but molecules (or indeed thin films) on the microresonator surface can also be detected. In particular, if the surface is covered to such an extent that the optical energy absorbed heats the microresonator, the resulting thermal bistability in the frequency-scan response can be used to determine the absorption and/or thickness of the thin-film coating. This and surface characterization by measurement of the thermal accommodation coefficient were described in Sect. 5.5. These methods offer quite precise measurement, provided that certain reasonable and easily implemented assumptions are satisfied.

In conclusion, when a WGM is excited in a dielectric microresonator, its evanescent component provides a convenient probe of the microresonator's surroundings. Various ways to implement evanescent-wave sensing have been devised, but the emphasis of this chapter has been on microcavity-enhanced absorption spectroscopy. The techniques described here have broad applicability, can even be used with broadband sources, and lend themselves well to further enhancement methods. We are looking forward to continuing our development of these sensors.

References

1 Matsko, A. B.; Ilchenko, V. S., Optical resonators with whispering-gallery modes – Part I: Basics, *IEEE J. Sel. Top. Quantum Electron.* **2006**, 12, 3–14

2 Ilchenko, V. S.; Matsko, A. B., Optical resonators with whispering-gallery modes – Part II: Applications, *IEEE J. Sel. Top. Quantum Electron.* **2006**, 12, 15–32

3 Rosenberger, A. T., Analysis of whispering-gallery microcavity-enhanced chemical absorption sensors, *Opt. Express* **2007**, 15, 12959–12964

4 Farca, G.; Shopova, S. I.; Rosenberger, A. T., Cavity-enhanced laser absorption spectroscopy using microresonator whispering-gallery modes, *Opt. Express* **2007**, 15, 17443–17448

5 Rosenberger, A. T.; Dale, E. B.; Ganta, D.; Rezac, J. P., Investigating properties of surfaces and thin films using microsphere whispering-gallery modes, In Laser Resonators and Beam Control X; Kudryashov, A. V.; Paxton, A. H.; Ilchenko, V. S., Eds.; *Proc. SPIE* **2008**, 6872, 68720U

6 Teraoka, I.; Arnold, S.; Vollmer, F., Perturbation approach to resonance shifts of whispering-gallery modes in a dielectric microsphere as a probe of a surrounding medium, *J. Opt. Soc. Am. B* **2003**, 20, 1937–1946

7 Hanumegowda, N. M.; Stica, C. J.; Patel, B. C.; White, I.; Fan, X., Refractometric sensors based on microsphere resonators, *Appl. Phys. Lett.* **2005**, 87, 201107

8 Armani, A. M.; Vahala, K. J., Heavy water detection using ultra-high-Q microcavities, *Opt. Lett.* **2006**, 31, 1896–1898

9 Savchenkov, A. A.; Matsko, A. B.; Mohageg, M.; Maleki, L., Ringdown spectroscopy of stimulated Raman scattering in a whispering gallery mode resonator, *Opt. Lett.* **2007**, 32, 497–499

10 Boyd, R. W.; Heebner, J. E., Sensitive disk resonator photonic biosensor, *Appl. Opt.* **2001**, 40, 5742–5747

11 Humphrey, M. J.; Dale, E.; Rosenberger, A. T.; Bandy, D. K., Calculation of optimal fiber radius and whispering-gallery mode spectra for a fiber-coupled microsphere, *Opt. Commun.* **2007**, 271, 124–131

12 Gorodetsky, M. L.; Ilchenko, V. S., Optical microsphere resonators: Optimal coupling to high-Q whispering-gallery modes, *J. Opt. Soc. Am. B* **1999**, 16, 147–154

13 Cai, M.; Painter, O.; Vahala, K. J., Observation of critical coupling in a fiber taper to a silica-microsphere whispering-gallery mode system, *Phys. Rev. Lett.* **2000**, 85, 74–77

14 Gorodetsky, M. L.; Ilchenko, V. S., High-Q optical whispering-gallery microresonators: Precession approach for spherical mode analysis and emission patterns with prism couplers, *Opt. Commun.* **1994**, 113, 133–143

15 Westcott, S. L.; Zhang, J.; Shelton, R. K.; Bruce, N. M. K.; Gupta, S.; Keen, S. L.; Tillman, J. W.; Wald, L. B.; Strecker, B. N.; Rosenberger, A. T.; Davidson, R. R.; Chen, W.; Donovan, K. G.; Hryniewicz, J. V., Broadband optical absorbance spectroscopy using a whispering gallery mode microsphere resonator, *Rev. Sci. Instrum.* **2008**, 79, 033106

16 Rosenberger, A. T.; Rezac, J. P., Whispering-gallery-mode evanescent-wave microsensor for trace-gas detection, In Biomedical Instrumentation Based on Micro- and Nanotechnology; Mariella, R. P., Jr.; Nicolau, D. V., Eds.; *Proc. SPIE* **2001**, 4265, 102–112

17 Rezac, J. P.; Rosenberger, A. T., Locking a microsphere whispering-gallery mode to a laser, *Opt. Express* **2001**, 8, 605–610

18 Chou, S.-I; Baer, D. S.; Hanson, R. K., Diode laser absorption measurements of CH_3Cl and CH_4 near 1.65 μm, *Appl. Opt.* **1997**, 36, 3288–3293

19 Boschetti, A.; Bassi, D.; Iacob, E.; Iannotta, S.; Ricci, L.; Scotoni, M., Resonant photoacoustic simultaneous detection of methane and ethylene by means of a 1.63-μm diode laser, *Appl. Phys. B* **2002**, 74, 273–278

20 Rothman, L. S.; Rinsland, C. P.; Goldman, A.; Massie, S. T.; Edwards, D. P.; Flaud, J.-M.; Perrin, A.; Camy-Peyret, C.; Dana, V.; Mandin, J.-Y.; Schroeder, J.; McCann, A.; Gamache, R. R.; Wattson, R. B.; Yoshino, K.; Chance, K. V.; Jucks, K. W.; Brown, L. R.; Nemtchinov, V.; Varanasi, P., The HITRAN molecular spectroscopic database and HAWKS (HITRAN atmospheric workstation): 1996 edition, *J. Quant. Spectrosc. Radiat. Transfer* **1998**, 60, 665–710

21 von Klitzing, W.; Long, R.; Ilchenko, V. S.; Hare, J.; Lefèvre-Seguin, V., Tunable whispering gallery modes for spectroscopy and CQED experiments, *New J. Phys.* **2001**, 3, 14.1–14.14

22 Farca, G., Cavity-Enhanced Evanescent-Wave Chemical Sensing Using Microresonators, PhD dissertation, Oklahoma State University, **2006**

23 Smith, D. D.; Chang, H.; Fuller, K. A.; Rosenberger, A. T.; Boyd, R. W., Coupled-resonator-induced transparency, *Phys. Rev. A.* **2004**, 69, 063804

24 Naweed, A.; Farca, G.; Shopova, S. I.; Rosenberger, A. T., Induced transparency and absorption in coupled whispering-gallery microresonators, *Phys. Rev. A* **2005**, 71, 043804

25 Shopova, S. I.; Blackledge, C. W.; Rosenberger, A. T.; Materer, N. F., Gold nanorods grown from HgTe nanoparticles directly on various surfaces, *Appl. Phys. Lett.* **2006**, 89, 023120

26 Shopova, S. I., Nanoparticle-Coated Optical Microresonators for Whispering-Gallery Lasing and Other Applications, PhD dissertation, Oklahoma State University, **2007**

27 Shopova, S. I.; Blackledge, C. W.; Rosenberger, A. T., Enhanced evanescent coupling to whispering-gallery modes due to gold nanorods grown on the microresonator surface, *Appl. Phys. B* **2008**, 93, 183–187

28 Il'chenko, V. S.; Gorodetskii, M. L., Thermal nonlinear effects in optical whispering gallery microresonators, *Laser Phys.* **1992**, 2, 1004–1009

29 Collot, L.; Lefèvre-Seguin, V.; Brune, M.; Raimond, J.-M.; Haroche, S., Very high-Q whispering-gallery mode resonances observed on fused silica microspheres, *Europhys. Lett.* **1993**, 23, 327–334

30 Carmon, T.; Yang, L.; Vahala, K. J., Dynamical thermal behavior and thermal self-stability of microcavities, *Opt. Express* **2004**, 12, 4742–4750

31 Malitson, I. H., Interspecimen comparison of the refractive index of fused silica, *J. Opt. Soc. Am.* **1965**, 55, 1205–1209

32 Rezac, J. P., Properties and Applications of Whispering-Gallery Mode Resonances in Fused Silica Microspheres, PhD dissertation, Oklahoma State University, **2002**

33 Carslaw, H. S.; Jaeger, J. C., Conduction of Heat in Solids, Clarendon, Oxford, **1959**, Chap. IX, 230–254

34 Foss, W. R.; Davis, E. J., Transient laser heating of single solid microspheres, *Chem. Eng. Commun.* **1996**, 152–153, 113–138

35 Kennard, E. H., Kinetic Theory of Gases, McGraw-Hill, New York, NY, **1938**, Chap. VIII, 291–337

36 Rogach, A. L.; Koktysh, D. S.; Harrison, M.; Kotov, N. A., Layer-by-layer assembled films of HgTe nanocrystals with strong infrared emission, *Chem. Mater.* **2000**, 12, 1526–1528

37 Saxena, S. C.; Joshi, R. K., Thermal accommodation and adsorption coefficients of gases, In Vol. II-1 of McGraw-Hill/CINDAS Data Series on Material Properties; Touloukian, Y. S.; Ho, C. Y., Eds.; McGraw-Hill, New York, NY, 1981

38 Vernooy, D. W.; Ilchenko, V. S.; Mabuchi, H.; Streed, E. W.; Kimble, H. J., High-Q measurements of fused-silica microspheres in the near infrared, *Opt. Lett.* **1998**, 23, 247–249

39 Rokhsari, H.; Spillane, S. M.; Vahala, K. J., Loss characterization in microcavities using the thermal bistability effect, *Appl. Phys. Lett.* **2004**, 85, 3029–3031